npj | imaging

Article

https://doi.org/10.1038/s44303-024-00011-9

In vivo imaging using surface enhanced spatially offset raman spectroscopy (SESORS): balancing sampling frequency to improve overall image acquisition

A list of authors and their affiliations appears at the end of the paper

In the field of optical imaging, the ability to image tumors at depth with high selectivity and specificity remains a challenge. Surface enhanced resonance Raman scattering (SERRS) nanoparticles (NPs) can be employed as image contrast agents to specifically target cells in vivo; however, this technique typically requires time-intensive point-by-point acquisition of Raman spectra. Here, we combine the use of "spatially offset Raman spectroscopy" (SORS) with that of SERRS in a technique known as "surface enhanced spatially offset resonance Raman spectroscopy" (SESORRS) to image deep-seated tumors in vivo. Additionally, by accounting for the laser spot size, we report an experimental approach for detecting both the bulk tumor, subsequent delineation of tumor margins at high speed, and the identification of a deeper secondary region of interest with fewer measurements than are typically applied. To enhance light collection efficiency, four modifications were made to a previously described custom-built SORS system. Specifically, the following parameters were increased: (i) the numerical aperture (NA) of the lens, from 0.2 to 0.34; (ii) the working distance of the probe, from 9 mm to 40 mm; (iii) the NA of the fiber, from 0.2 to 0.34; and (iv) the fiber diameter, from 100 µm to 400 µm. To calculate the sampling frequency, which refers to the number of data point spectra obtained for each image, we considered the laser spot size of the elliptical beam (6 × 4 mm). Using SERRS contrast agents, we performed in vivo SESORRS imaging on a GL261-Luc mouse model of glioblastoma at four distinct sampling frequencies: par-sampling frequency (12 data points collected), and over-frequency sampling by factors of 2 (35 data points collected), 5 (176 data points collected), and 10 (651 data points collected). In comparison to the previously reported SORS system, the modified SORS instrument showed a 300% improvement in signal-to-noise ratios (SNR). The results demonstrate the ability to acquire distinct Raman spectra from deep-seated glioblastomas in mice through the skull using a low power density (6.5 mW/mm^2) and 30-times shorter integration times than a previous report (0.5 s versus 15 s). The ability to map the whole head of the mouse and determine a specific region of interest using as few as 12 spectra (6 s total acquisition time) is achieved. Subsequent use of a higher sampling frequency demonstrates it is possible to delineate the tumor margins in the region of interest with greater certainty. In addition, SESORRS images indicate the emergence of a secondary tumor region deeper within the brain in agreement with MRI and H&E staining. In comparison to traditional Raman imaging approaches, this approach enables improvements in the detection of deep-seated tumors in vivo through depths of several millimeters due to improvements in SNR, spectral resolution, and depth acquisition. This approach offers an opportunity to navigate larger areas of tissues in shorter time frames than previously reported, identify regions of interest, and then image the same area with greater resolution using a higher sampling frequency. Moreover, using a SESORRS approach, we demonstrate that it is possible to detect secondary, deeper-seated lesions through the intact skull.

e-mail: fay_nicolson@dfci.harvard.edu

In the field of medical imaging, the ability to detect deep-seated tumors in real time is both necessary and challenging. Utilizing light as an excitation source, optical imaging encompasses techniques including fluorescence, bioluminescence, optoacoustics, and Raman spectroscopy[1,2]. Optical imaging modalities can provide real-time, high-resolution visualization and characterization of structures and biological processes at the cellular and molecular level. This, together with its relatively low cost, high throughput, high spatial resolution, and ability to provide molecularly specific information, makes optical imaging modalities highly suitable for applications involving real-time imaging of cancer in vivo[3]. Currently, fluorescence based approaches lead the way in optical molecular- and intraoperative-imaging[2,4–7], however, fluorescence suffers from photobleaching and intrinsic autofluorescence[8]. Furthermore, fluorescent agents often exhibit broad and overlapping emission bands, which can restrict their utility in multiplexing applications[6].

Raman spectroscopy is a high-resolution, non-destructive optical molecular imaging strategy which relies upon the collection of inelastic light scattering following excitation with a laser source[9]. Its applicability in its intrinsic form (i.e. without the use of any contrast agent) has been demonstrated extensively in a number of biomedical applications including in vivo imaging[9–11] and image guided surgery in patents with grade 2 to 4 gliomas[12]. However, while such an approach successfully enables the discrimination between the different tissue types, e.g. healthy or cancerous, intrinsic Raman spectroscopy is often associated with poor signal to noise ratios (SNR), long acquisition times, and typically relies on post-processing methods to deconvolute the spectra information, therefore hindering its potential for use for in vivo applications[13,14]. Nanoparticle (NP) based contrast agents (CAs) in the form of surface enhanced Raman scattering (SERS) NPs and surface enhanced resonance Raman scattering (SERRS) NPs have thus been employed to in part, circumvent the aforementioned limitations.

SERRS CAs are often composed of a core-shell structure which consist of a gold nanoparticle core functionalized with a resonant Raman reporter, which is then encapsulated in a silica shell[15,16]. By tracking their unique "fingerprint" spectra, SERRS CAs can be used to image tumors by targeting cells with high specificity in vivo (e.g. using antibodies[17–20] or peptides[21,22]). Non-targeted SERRS CAs have also been shown to accumulate in solid tumors due to the enhanced permeability and retention (EPR) effect[14,16,23–25] with several reports demonstrating the reliable detection of a large variety of different tumor types in vivo *using* SERRS CAs, including microscopic (<100 μm) and their microscopic extensions using SERRS NPs[15–18,21,26]. Unlike fluorescence imaging, SERRS imaging allows the visualization of a large number of molecular markers within the same tumor sample simultaneously due to the unique "fingerprint" spectra of each "flavor" of SERRS CAs[6,25,27].

Despite several reports in the literature demonstrating the applicability of SERRS CAs to cancer imaging, the approach is largely limited to surface-based lesions due to the principal of light scattering in turbid media, including biological tissue. Spatially offset Raman spectroscopy (SORS) is an emerging optical molecular imaging approach which takes advantage of light-scattering properties of tissue to enable the visualization of deep-seated region(s) of interest (ROI) such as malignant tumors[28], while also suppressing autofluorescence contributions from the tissue[29,30]. The approach capitalizes on the statistical phenomenon whereby photons originating from deeper within a medium exhibit a greater propensity for lateral migration away from the point of illumination compared to their surface-level counterparts[29,30], thus light is scattered in multiple directions before it is gathered by the collection optics[30–32]. Surface enhanced spatially offset resonance Raman spectroscopy (SESORRS) describes the use of SORS to detect the accumulation of SERRS CAs in an ROI and offers the potential to image cancer with high contrast in vivo at depths far superior to what can currently be achieved using other optical imaging approaches[30,31,33,34]. SESORRS has been shown to successfully detect the accumulation of SERRS CAs through depths of up to 14 cm[35–37]. Recently, SESORRS has been applied to a number of biomedical applications including the detection of neurotransmitters[38,39], ex vivo breast cancer tumor models and phantoms[35,40,41], and the detection of glioblastoma in vivo[26].

The scientific literature contains studies investigating the application of SERS (Surface-Enhanced Raman Scattering) and SERRS (Surface-Enhanced Resonance Raman Scattering) nanotags for intra-operative cancer imaging in vivo, employing conventional confocal Raman spectroscopy techniques. Additionally, SESORS (Surface-Enhanced Spatially Offset Raman Spectroscopy) and SESORRS has been explored for probing clinically relevant depths, both ex vivo and in phantom models[35,36,40,41]. However, there are very few reports on the use of SESORRS for imaging of disease in vivo[28] and none on the application of sampling frequency approaches to increase the overall speed of image acquisition over a ROI in a biological subject. Here we report for the first time, an experimental SESORRS approach for detecting both the bulk tumor and subsequent high-speed delineation of tumor margins, with fewer measurements than typically applied. This was achieved through optimization of a custom-built SORS probe which generated significantly higher SNRs in comparison to the previous set up. The custom-built collection probe was used to image the accumulation and uptake of Raman active SERRS nanotags in a GL261 mouse model of glioblastoma (GBM). Previously, our group demonstrated the first application of the SESORRS approach for the imaging of GBM through the intact skull, however this approach used long acquisition and accumulation times, higher laser powers, and did not consider sampling frequency[28]. By improving our collection efficiency through the engineering of a custom built SORS collection probe, significant reduction in integration time, and utilization of sampling frequency approaches, we report the successful detection of GBM though the intact skull in as little as 6 s. In doing so, we demonstrate a means to detect a ROI and then delineate the ROI with greater certainty and improved resolution. In addition, SESORRS imaging detected the emergence of a secondary ROI deeper within the brain, in agreement with MRI and H&E staining, thus suggesting the suitably of SESORRS as intraoperative imaging approach for the detection and imaging of deep-seated tumors.

Results

Our previous report of the use of SESORRS for the in vivo imaging of disease involved a commercially available collection probe to collect the scattered spatially offset photons. Although we successfully demonstrated the suitability of the approach, there were several limitations. Limitations included a short working distance from the sample surface and poor SNR, which in turn meant we had to utilize longer acquisition times and higher laser powers that reduced the applicability of our approach to in vivo imaging applications. To address these limitations and increase light collection efficiency, we built our own SORS collection probe, as described in the methods section. In comparison to the commercially available probe, we applied four optimizations to our custom-built probe: (i) numerical aperture (NA) of the lens (0.2 to 0.34), (ii) working distance of the probe (9 mm to 40 mm), (iii) NA of the fiber (0.2 to 0.34), and (iv) fiber diameter (100 μm to 400 μm). The internal optics of the collection probe are described in Fig. 1A and the final probe is shown in Fig. 1B. In this case, we made a strategic choice to incorporate 45° filters rather than 0° filters, as we aimed to enhance the ability of our custom probe to filter out both Raleigh and stray light. Due to the reflective nature of interference filters, the utilization of a normal or near-normal incidence filter presents a potential drawback given that these filters have the tendency to reflect light back toward the sample, initiating a cycle where the reflected light could be recycled back into the probe. Since these filters are not 100% reflective, the more recycled light present ultimately increases the amount of unwanted light that passes into the spectrometer. The incorporation of a filter angled at 45° helps to redirect unwanted light into the cage-cube and this intentional angling helps to prevent Rayleigh and stray-light from passing upstream into the spectrometer. Because the use of a single filter at 45° results in a large shift of the optical axis which would negatively impact overall collection efficiency, we used a second 45° filter angled in the opposite direction to "walk the beam" back into the original optical axis.

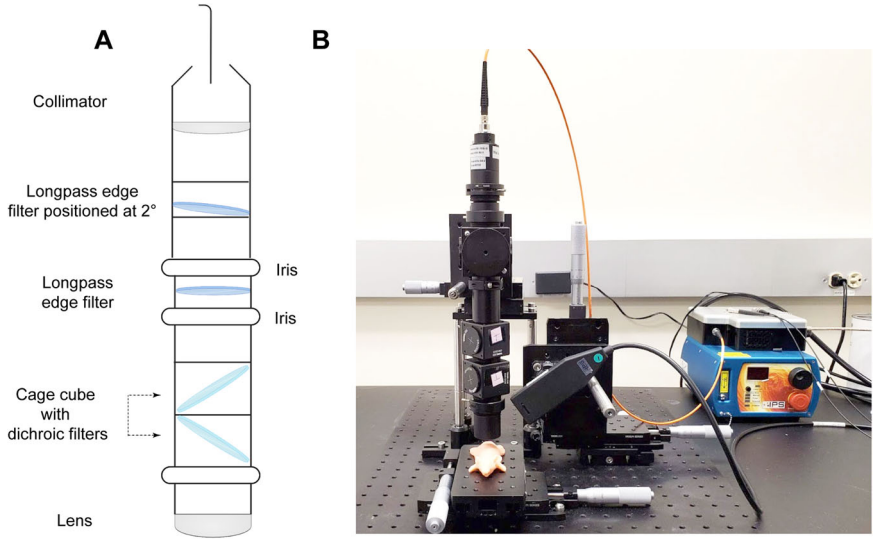

Fig. 1 | SORS Set-up using the custom-built probe. **A** Diagram describing the internal optics of the custom-built SORS collection probe. **B** In-house SORS set-up using the custom-built probe with an optical mouse phantom placed on the *xy* stage. Incident light is delivered at 45° to the sample surface and light is collected through the custom-built collection probe.

Taken together, this dual filter approach helps to mitigate stray light interference and improve SNR.

To evaluate the efficiency of the new custom-built probe in comparison to the previously used probe, we used plastic calibration standards. Sheets of pink polypropylene (PP) were placed on top of a Polytetrafluoroethylene (PTFE) layer to create a barrier with the aim of detecting the PTFE analyte through the PP barrier (Fig. S1). Spectra of PTFE through PP thicknesses of 8, 14 and 20 mm of PP were acquired using the commercially available and custom-built SORS systems with spatial offsets of 0 to 10 mm (1 mm increments) The peak intensity of 739 cm^{-1} obtained through these thicknesses using either probe is shown in (Fig. 2A–C). The 739 cm^{-1} peak was chosen, since it represents the most intense peak in the PTFE spectrum (Fig. S1B). In both probe configurations, as the thickness of the polypropylene (PP) barrier increases, a larger spatial offset is necessary to achieve the highest polytetrafluoroethylene (PTFE) signal through the increased thicknesses. Notably, the custom-built probe consistently produces a higher signal than the commercially available probe across all tested thicknesses and offsets. Fig. 2D–F describes the SNRs of each probe at 0–10 mm offsets through the same three thicknesses of plastic (8, 14 and 20 mm). As expected, the custom probe generates significantly higher SNRs through each of the three thicknesses. Fig. 2C shows similar contribution of signal using the commercially available probe through 20 mm of PP at 0–10 mm offsets which is attributed to noisy spectra (i.e., the PTFE cannot be detected). This is confirmed in Fig. 2F, which shows that the SNR for the commercial probe is consistently below 3. In contrast, our custom-built probe demonstrates the ability to detect PTFE through 20 mm of PP. As the thickness of the PP barriers increases, there is a notable reduction in both the SNRs and the relative intensity of the PTFE peaks. This decrease can be attributed to photon migration and energy loss, regardless of whether a commercially available probe or a custom-built probe is used. Furthermore, the data clearly indicates that as the PP barrier thickness increases, larger spatial offsets are necessary in order to achieve a significant spectral contribution from the PTFE. By increasing the spatial offset – specifically, the distance between the excitation spot and the collection point – it becomes possible to clearly discern the spectral contribution of PTFE through the PP barrier. These results indicate that our custom-built collection probe, which replaces the commercially available probe, has effectively improved our SORS system. We have achieved these enhancements due to increased Raman throughput and higher SNRs.

Having demonstrated the efficiency of our custom-built collection probe over the commercially available probe, we sought to reduce the overall time taken to sample an ROI by investigating the impact of sampling frequency on in vivo SESORRS imaging. Imaging approaches using conventional Raman approaches apply a tightly focused beam to achieve high resolution images, however, this technique typically requires time-intensive point-by-point acquisition of Raman spectra, hindering the real-time image acquisition desired for clinical applications. When imaging an ROI using Raman spectroscopy, the resulting image is not only a function of the laser spot size, but also of the distance between the sequentially scanned locations referred to as the sampling step or pixel size. There are three principal relationships between the laser spot and the sampling step: under-sampling, par-sampling, and over-sampling. Par-sampling, which involves matching the sampling step to the laser spot, provides an adequate estimation of the ROI, whereas over-sampling (where the step size is smaller than the laser spot size) has been shown to provide a significant improvement in image quality at the expense of total image acquisition time, given that the time taken to over-sample an ROI will be significantly higher than using a par-sampling approach on the same ROI[43–45]. In comparison to conventional Raman approaches, which typically utilize a laser beam with a spot size on the micron scale, SORS approaches typically employ a laser beam with a spot size on the mm-cm scale[30]. Therefore, by taking advantage of sampling frequency approaches and increased laser-spot size and sampling frequency, we hypothesized that by using a smaller sampling frequency approach, it would be possible to image a significantly larger area in a shorter time frame in comparison to Raman approaches utilizing a tightly focused beam.

Sampling step size is determined by the laser spot size with a par-sampling frequency having the same steps size as the laser diameter in *x* and *y* and an over-sampling approach having a step size smaller than the laser diameter. Given that sampling frequency will influence the overall resolution of an image (i.e., a higher sampling frequency should delineate an ROI with greater certainty due to the acquisition of a greater number of data points from given area) we wanted to investigate how this could be applied to SESORRS imaging to reduce the overall time take to image an ROI. Calculations of the sampling frequency, or the number of spectral data points obtained per image, were performed based on the laser spot size of the elliptical beam, which measures 6 mm×4 mm (Fig. 3A). For par sampling, a step size of 6 mm in the *x*-direction and 4 mm in the *y*-direction is required. In the case of over-sampling by a factor of 10, the step sizes would need to be reduced to 0.6 mm in the *x*-direction and 0.4 mm in the *y*-direction. It is important to note that the sampling frequency directly impacts the overall resolution of the resulting image. In this study, we explored the effects of both par-sampling and over-sampling at frequencies of 2, 5, and 10, as illustrated in Fig. 3, across a 12 mm × 12 mm area. Therefore, if we were to sample an area of 12 × 12 mm using each of the four sampling frequency

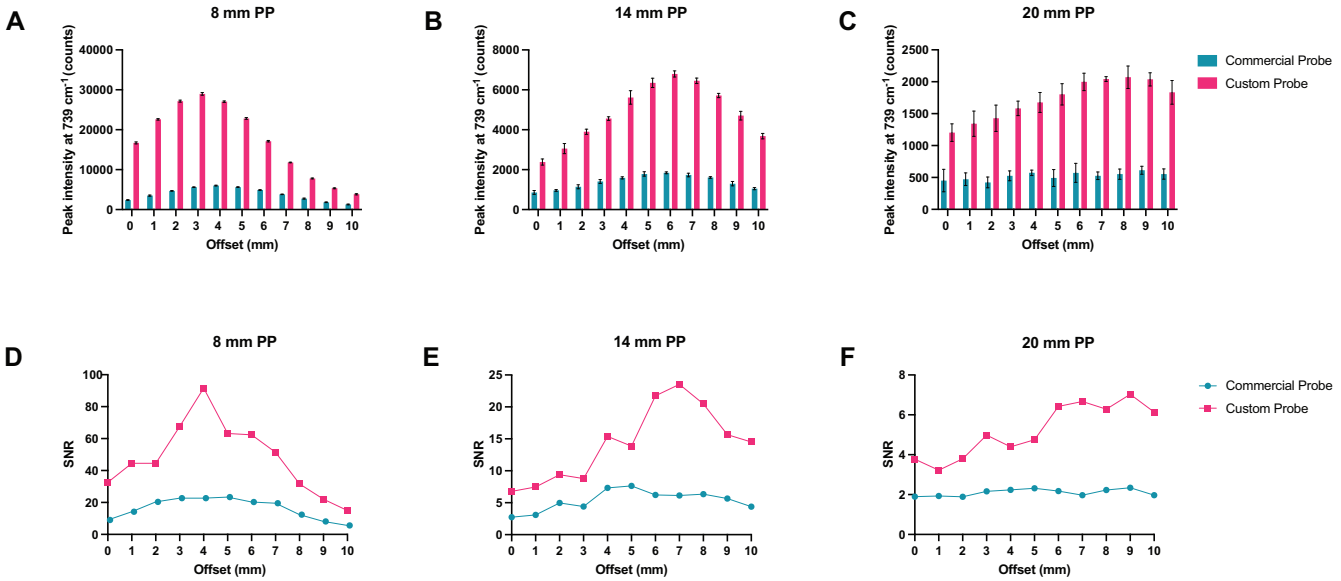

Fig. 2 | Comparison of the collection efficiencies of the commercially available collection probe and the custom-built collection probe. A–C Peak intensity of PTFE at 739 cm^{-1} through 8, 14, and 20 mm of polypropylene (PP) at 0–10 mm spatial offsets (1 mm increments). **D–F** Comparison of signal-to-noise ratios from each probe through 8, 14, and 20 mm of PP at 0–10 mm spatial offsets (1 mm increments). Spectra were acquired using a 4 s integration, 5 acquisitions, 785 nm laser, 500 mW laser power.

approaches (par-sampling, over-sampling by 2, 5, and 10), we would need to perform a total of 12, 35, 176, and 651 measurements respectively, to create our image (Fig. 3B–E). The step-size in *x* and *y* for each sampling frequency is summarized in Table 1. We hypothesized that in comparison to a par-sampling frequency approach, over-sampling by a small number (e.g., 2 and 5) would give rise to higher resolution images; however, further increases in the sampling frequency (e.g., 10) would not generate a significant increase in image contrast. Moreover, a higher sampling frequency would result in an increase of total time taken to image an ROI. Thus we sought to investigate the influence of sampling frequency approach on image quality.

To investigate the influence of sampling frequency on image quality, we prepared a brain-tumor phantom that was representative of an in vivo GBM. Briefly, the brain of a 12 week old-euthanized mouse was removed, and the skin over the face of the mouse left intact. The head was then fixed in 4% PFA and then transferred to 70% EtOH. PTFE (5 mm × 5 mm, thickness 2 mm) was glued directly underneath the skull to create a brain tumor mimic (Fig. 4A) and then filled with agarose gel. Unlike previous work where the skin of the mouse was removed from the head and we wrapped the skull in porcine tissue to create a skin mimic, only fur was removed using hair removal cream and the skin was left on the mouse's head (Fig. 4B). The mouse head was placed on a paraffin wax mold (Fig. 4B) to allow repeated measurements of the head over multiple days by ensuring the mouse head was continually placed in the same position as the prior day. The mapping of PTFE through the mouse head was then carried out at spatial offset of 1–3 mm, 0.5 mm increments. The spatial offset was controlled by moving the *xyz* translational stage away from the point of collection. The spatial offset was kept fixed for each set of measurements, and the sample was moved using the *xy* stage (i.e., the excitation and collection optics remained static at each spatial offset). Measurements were taken at varying step sizes depending on the sampling frequency being used (Table 1). Surface/contour false color 2D heat maps were then constructed using the peak height of PTFE (739 cm^{-1}).

Figure 4 demonstrates the mapping of the brain tumor phantom using each of the four sampling frequencies at spatial offsets of 1 mm (Fig. 4C–F), 1.5 mm (Fig. 4G–J), 2 mm (Fig. 4K–N), 2.5 mm (Fig. 4O–R), and 3 mm (Fig. 4S–V). In this case, over-sampling by 10 at a 1.5 mm spatial offset gave rise to the highest signal, thus all other images were normalized to the most intense peak in this image. As shown in Fig. 4, when the sampling frequency is increased, the ability to delineate the PTFE square is also improved. As anticipated, the difference in image quality between images acquired using a sampling frequency of 5 and 10 is subtle, indicating that there may be limited advantages to using a higher sampling frequency approach. Encouragingly, the area of intensity that corresponds to the PTFE signal is in agreement with the size of PTFE that was glued beneath the mouse's skull (5 mm × 5 mm). In previous work, we demonstrated the detection of PTFE through a brain tumor where the skin was removed from the mouse's head, PTFE embedded underneath the skull and the head then wrapped in 2 mm of porcine tissue and imaged using a SORS approach at 2, 2.5, and 3 mm spatial offset, 1 mm step sizes[28]. In comparison to our previous work, by over-sampling by 5 and by 10 we demonstrate improved delineation of PTFE at 1, 1.5, 2-, 2.5-, and 3-mm spatial offsets. In this work, even at lesser sampling frequencies (i.e., par and 2), we demonstrate successful detection of a rough ROI and therefore hypothesize that we could use such sampling frequency to scan large areas of tissue, identity ROIs, and then delineate these areas with greater certainty using a larger sampling frequency approach in vivo. Our data indicate that a spatial offset of 1.5 mm is particularly suitable for in vivo SESO(R)RS imaging of GBM using our custom-built collection optics. This offset effectively suppresses surface signals, as evidenced by the reduction in spectral contributions from tissue and bone peaks at 1440 cm^{-1} and 957 cm^{-1}, respectively. Moreover, it produces a strong contribution from PTFE at 739 cm^{-1}, resulting in both high SNRs and intense signal. In our decision to proceed with a 1.5 mm spatial offset, we are confident that any of the five spatial offsets under consideration would have been apt for in vivo imaging. Furthermore, considering that the selection of spatial offset is contingent on the specific sample, and that the depth of an analyte frequently remains unknown, our findings indicate that it is feasible to capture images of a ROI at different spatial offsets without substantially affecting the overall image quality. This capability is especially valuable for in vivo imaging, where tumor growth is inherently three-dimensional and the extent of tumor invasion may not be comprehensively characterized before imaging.

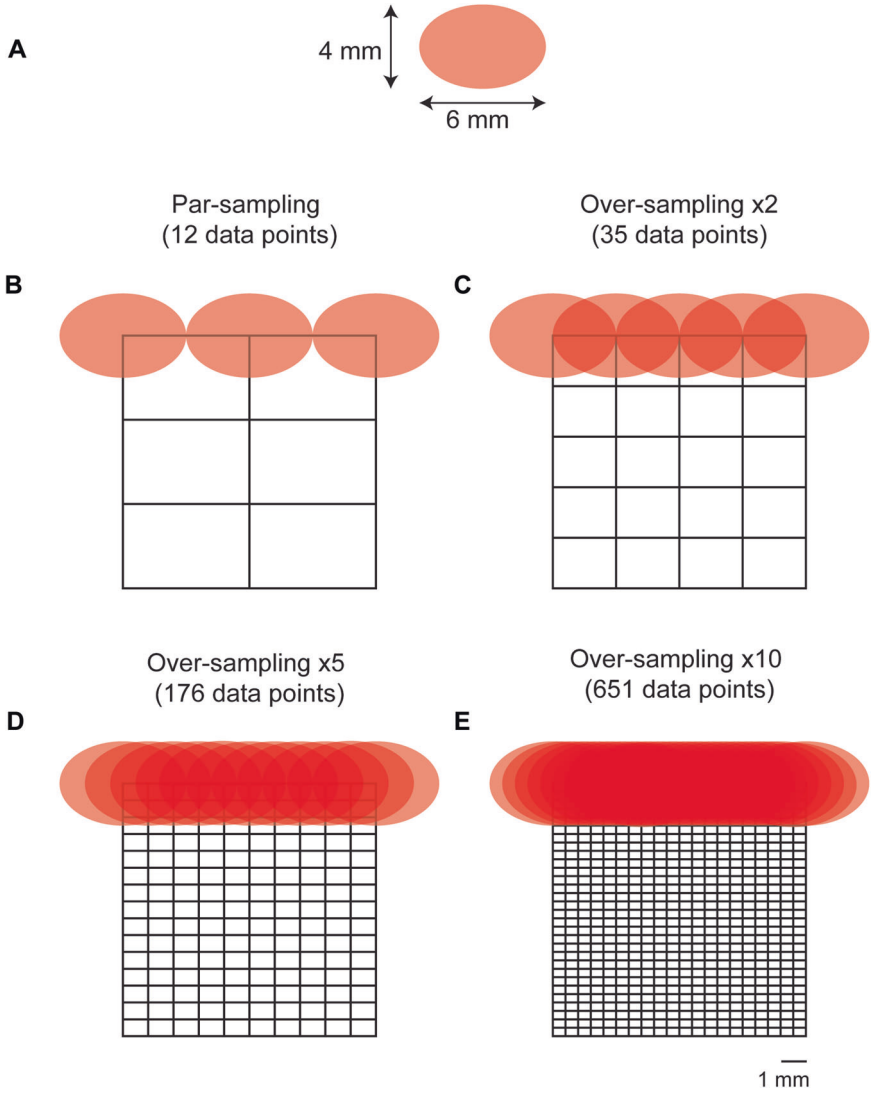

Fig. 3 | Diagram demonstrating par-sampling and over-sampling by 2, 5 and 10 over a 12 × 12 mm area. A Laser spot-size. The beam is elliptical and thus has a diameter of 6 mm×4 mm. (B-E) diagram demonstrating the number of measurements per sampling frequency of a 12 × 12 mm area. Par sampling represents a step size of 6 mm in × and 4 mm in y, whereas a ×10 sampling frequency represents a 0.6 mm step size in *x* and a 0.4 mm step size in *y*. Stepwise measurements are performed in *x* and then in *y* to image the whole 12 × 12 mm area. **B** Par-sampling approach resulting in a total of 12 data points collected over the ROI. **C** Over-sampling by 2 resulting in a total of 35 data points collected over the ROI. **D** Over-sampling by 5 resulting in a total of 176 data points collected over the ROI. **E** Over-sampling by 10 resulting in a total of 651 data points collected over the ROI.

Table 1 | Summary of step sizes applied to each sampling frequency and the total number of data points collected across a 12 × 12 mm area.

Sampling frequency	Step-size in *x* (mm)	Step-size in *y* (mm)	Total number of data points
Par	6	4	12
Oversampling ×2	3	2	35
Oversampling ×5	1.2	0.8	176
Oversampling ×10	0.6	0.4	651

Building on our proof-of-concept measurements using brain tumor phantoms, we then proceeded with in vivo studies using SERRS CAs (Fig. 5A). SERRS CAs were synthesized using gold nanostars which were functionalized with a resonant Raman reporter molecule (IR780p) and encapsulated in a silica shell. The silica shell was then functionalized with PEG_{5000} to increase their biocompatibility (Fig. 5A). For this work, we chose a commercially available near-IR active dye (IR780p) due to its resonance properties. Such properties ensure the greatest enhancement of Raman signal following interaction of the SERRS CAs with incident light (785 nm). The corresponding SERRS spectrum of the SERRS CAs is shown in Fig. 5B. SERRS CAs were also characterized by zeta potential analysis, nanoparticle tracking, and TEM (Fig. 5C). The final SERRS CAs used in this study had a diameter of 133 ± 12 nm, as confirmed by TEM. The zeta potential of the SERRS CAS was −48 mV after thiolation and −15 mV after pegylation indicating successful functionalization of SERRS CAs with PEG_{5000}. Following synthesis, SERRS CAs were injected via the tail vein to GBM tumor-bearing BALB/cJ mice. Tumor incidence and size was confirmed by MRI at 2 weeks post intracranial injection of GL261-Lu cells, Fig. 6A–C. In this instance SERRS CAs were not functionalized with a targeting ligand, thus we relied solely on the EPR effect to ensure uptake of the NPs at the ROI. Previous work from our group has demonstrated the successful targeting of various solid tumors in vivo using targeted SERRS CAs; thus, the purpose of this

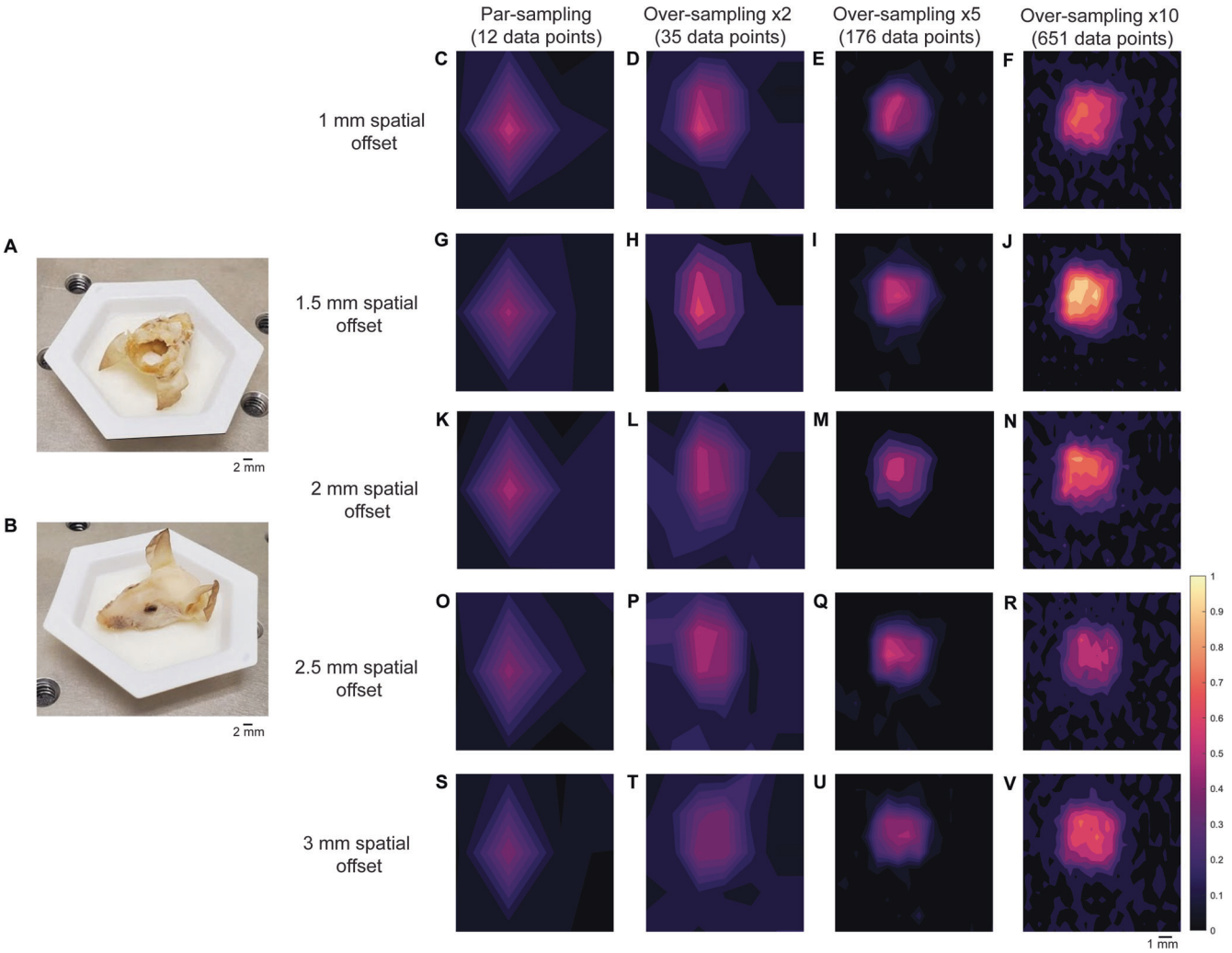

Fig. 4 | Application of varying sampling frequency approaches (par, ×2, ×5 and ×10) in brain tumor phantoms at 1–3 mm spatial offsets (0.5 mm increments). **A** PTFE placed under the mouse's skull. **B** Mouse head placed in paraffin wax mold. **C–F** Mapping of the brain tumor phantom at using a par-sampling frequency and oversampling by 2, 5, and 10 at a 1 mm spatial offset. **G–J** Mapping of the brain tumor phantom using a par-sampling frequency and oversampling by 2, 5, and 10 at a 1.5 mm spatial offset. **K–N** Mapping of the brain tumor phantom using a par-sampling frequency and oversampling by 2, 5, and 10 at a 2 mm spatial offset. **O–R** Mapping of the brain tumor phantom using a par-sampling frequency and oversampling by 2, 5, and 10 at a 2.5 mm spatial offset. **S–V** Mapping of the brain tumor phantom using a par-sampling frequency and oversampling by 2, 5, and 10 at a 3 mm spatial offset. All measurements were acquired using the custom-built collection probe, 785 nm laser, 0.5 s integration time, 1 accumulation.

work was not to evaluate potential targeting ligands, but to demonstrate the potential of SESORRS imaging for the detection and delineation of ROIs in vivo and improve the overall collection efficiency of our approach. In our previous report using SESORRS for the imaging of GBM, we used targeted SERRS CA with a concentration of 8 nM[28]. In this work, however, we used due to optimization of the NP synthesis protocol from previous reports and optimization of the collection probe, we were able to reduce the concentration of the injected dose to 2 nM, demonstrating a significant improvement on previous reports on the use of SERRS CAs for in vivo imaging using SESORRS[28]. Biodistribution studies on the uptake of SERRS CAs in vivo confirmed the accumulation of NPs in the liver, spleen, and lymph nodes (Fig. S3) which is consistent with other reports involving SERRS nanoparticles[14,15,26,28,46]. It is well recognized that most systemically administered SERRS CAs with diameters greater than 100 nm are retained by primary tissues associated with the reticuloendothelial system (RES), i.e., liver, spleen, and lymph nodes[47,48]. Moreover, it is hypothesized that fewer than 1% of systemically administered NPs reach the target, i.e., tumor[49,50]. Smaller SERRS CAs are of course preferrable to reduce RES uptake, however this is at the expense of decreased SERRS signal. While this work did not investigate the long-term toxicity of SERRS CAs, previous work by Gambhir and colleagues has shown that after intravenous injection via the tail vein, pegylated SERRS CAs elicit a mild inflammatory response an increase in oxidative stress in the liver 24 h post injection in rodent models[47]. Of note, the inflammatory response did subside over a two-week period following injection. Measurement of clinical, histological, biochemical, and cardiovascular parameters over the same two-week period also suggested no evidence of significant toxicity[47]. Importantly, other studies using SERRS CAs with similar diameters to the ones reported here, have demonstrated that oral[51], as well as topical administration[17,18] prevents systemic uptake in vivo. Thus, depending on the intended target organ, these could serve as viable alternative routes of administration for future SESORRS applications.

The application of varying sampling frequency approaches to the imaging of GBM through the intact skull using a SESORRS approach is described in Fig. 6. MR images taken prior to SESORRS imaging confirm the presence of a left frontal tumor at a depth of 2.5 mm and, interestingly, the emergence of a secondary ROI at deeper depths is also observed via MRI at depths of 3.5 and 4.25 mm (Fig. 6B, C respectively).

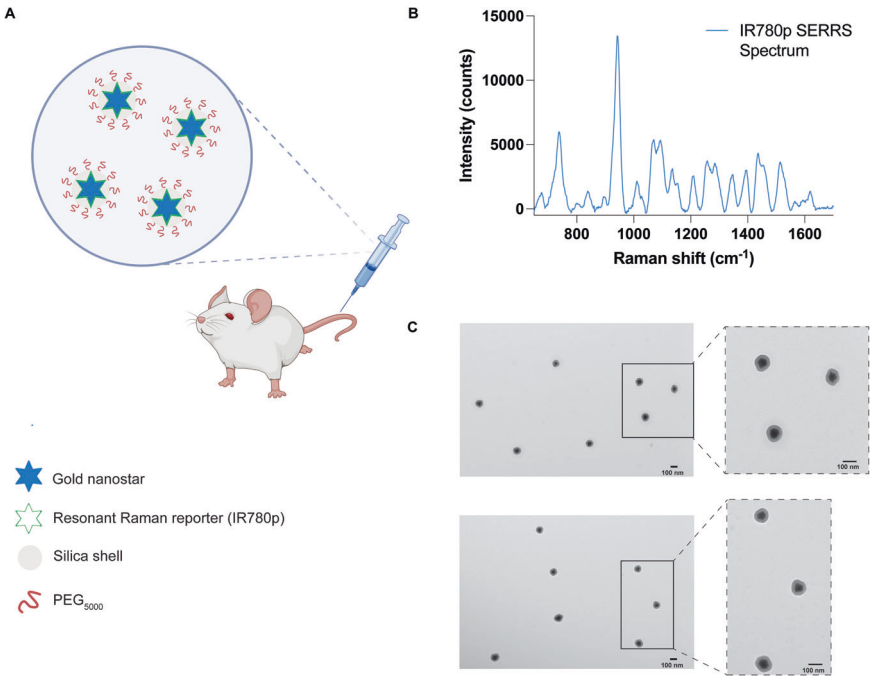

Fig. 5 | Characterization of SERRS nanostars for in vivo administration. A Conceptual figure showing gold nanostars administered via the tail vein. Gold nanostars were functionalized with a resonant Raman reporter molecule (IR780p) and then encased in a silica shell which was then functionalized with PEG_{5000}. **B** The unique fingerprint spectrum of the SERRS nanostars functionalized with IR780p. The spectrum corresponds to that of IR780p. SERRS spectra were obtained using a 785 nm wavelength, 100 ms integration time. **C** Transmission electron microscope image of the PEGylated SERRS nanostars from two different areas on the TEM grid. The scale bar represents 100 nm. Together the nanostars and silica shell had a total average diameter of 133 ± 12 nm. Images were acquired using a JEOL 1200EX Transmission Electron Microscope at 80 kV.

Subsequent SESORRS imaging was then performed using a par-sampling frequency and over-sampling frequencies of 2, 5, and 10 over the same area on each mouse (Fig. 6D–G). Images were constructed following application of PCA and principal components 2 and 3 were folded to a spectral image. The total aquistion time (6 s, 17.5 s, 88 s, and 325 s) at each frequency is also indicated. Background removal of areas of non-intensity were then subtracted from the SESORRS images (Fig. 6H–K) and the images were then rotated anti-clockwise (−20°) to match the orientation of the magnetic resonance (MR) images. As sampling frequency increases the ability to delineate the ROI is increased, however there is little difference in resolution between the images acquired using an over-sampling frequency of 5 and 10, thus suggesting that such extreme sampling frequencies are not necessary for in vivo SESORRS imaging. To better understand the degree of difference in images obtained at each sampling frequency, we applied structural similarity index (SSIM) calculations. SSIM considers changes in the texture, luminance, and contrast, of an image, rather than just pixel-by-pixel differences[52]. SSIM values range from −1 to +1, where +1 indicates that the two images being compared are identical, and −1 indicates that there is no structural similarity whatsoever. Using the SSIM matrix, we show that all SESORRS in vivo images retain a certain level of similarity to each other, with images obtained using a sampling frequency of 5 and 10 being the most similar pair. The SSIM matrix, and corresponding values are shown in the supporting information in Table S1 and Fig. S4. In addition to improved image resolution, the emergence of a secondary ROI with lower spectral intensity is also observed at all four sampling frequencies, indicating that our SESORRS approach is able to detect deeper seated lesions and also to detect signal that is proportional to depth. This is in agreement with the theory of photon migration in tissue (i.e., deeper born photons will give rise to lower intensity signal). Sample spectra taken at points of maximum and minimum intensity from the respective image using a par-sampling frequency and an over-sampling frequency of 2, 5 and 10 respectively are also shown (Fig. 6L–O). In all four cases, the data clearly demonstrate the detection of SERRS CAs in the pixels of maximum intensity due to detection of several peaks related to IR780p including the main peak at 947 cm^{-1} which is attributed to IR780p (i.e., the resonant Raman reporter used in this study). Spectra taken at the point of minimum intensity show spectral contribution solely from tissue (e.g., 1440 cm^{-1}), indicating selective uptake of the SERRS CAs within the tumor and not in healthy tissues. Ex vivo H&E staining also confirmed the presence of a tumor and emergence of a secondary tumor region as deeper regions of the brain are sliced (Fig. 6P–R). Moreover, the histopathological findings were also in agreement with the MR images which were taken prior to SESORRS imaging (Fig. 6A–C).

Discussion

The main aim of this study was to develop a more efficient SORS imaging system and approach in order to reduce the overall time take to image a ROI. In our previous report, we used a 15 s integration time, (3 s, 5 acquisitions) which resulted in lengthy image acquisition at each data point. In this work however, we utilized a 0.5 s integration time and 1 acquisition at each data point, demonstrating a significant improvement in the collection efficiency of our custom-built SORS collection probe (30-times shorter integration time per acquisition point). The ability to map the whole head of the mouse and determine a specific region of interest using as few as 12 spectra (total acquisition time 6 s) is achieved and we demonstrate that the subsequent use of a higher sampling frequency can delineate tumor margins in the ROI with greater certainty (Fig. 6D–K). Similarly, in comparison to our previous report, we have also been able to lower the integration time used for the detection of GBM using a SESORRS approach from 13.8 mW/mm^2 to 6 mW/mm^2[2,28]. Using the American National Standard for the Safe Use of Lasers (ASNI) Z136 as a reference, we calculated the MPE for skin exposure to a laser beam. Considering the experimental parameters for in vivo SESORRS imaging presented in this work, we calculated the MPE to be 1.368 J/cm^2. Subsequent consideration of the power density corresponding to our laser spot size, specifically at 0.3 J/cm^2, demonstrates that our power density is well within the established MPE limit for skin exposure as defined by ASNI. However, we point out that MPEs are set for accidental exposure to radiation and not for intentional exposure, e.g., for use in a clinical and cosmetic procedures. Therefore, the clinical limit could, and most likely would, differ when considering the benefit to the patient.

In addition to lowering the overall time taken to image an ROI, and perhaps most importantly, this work demonstrates the possibility to delineate a secondary ROI deeper within the brain using our SESORRS approach at all

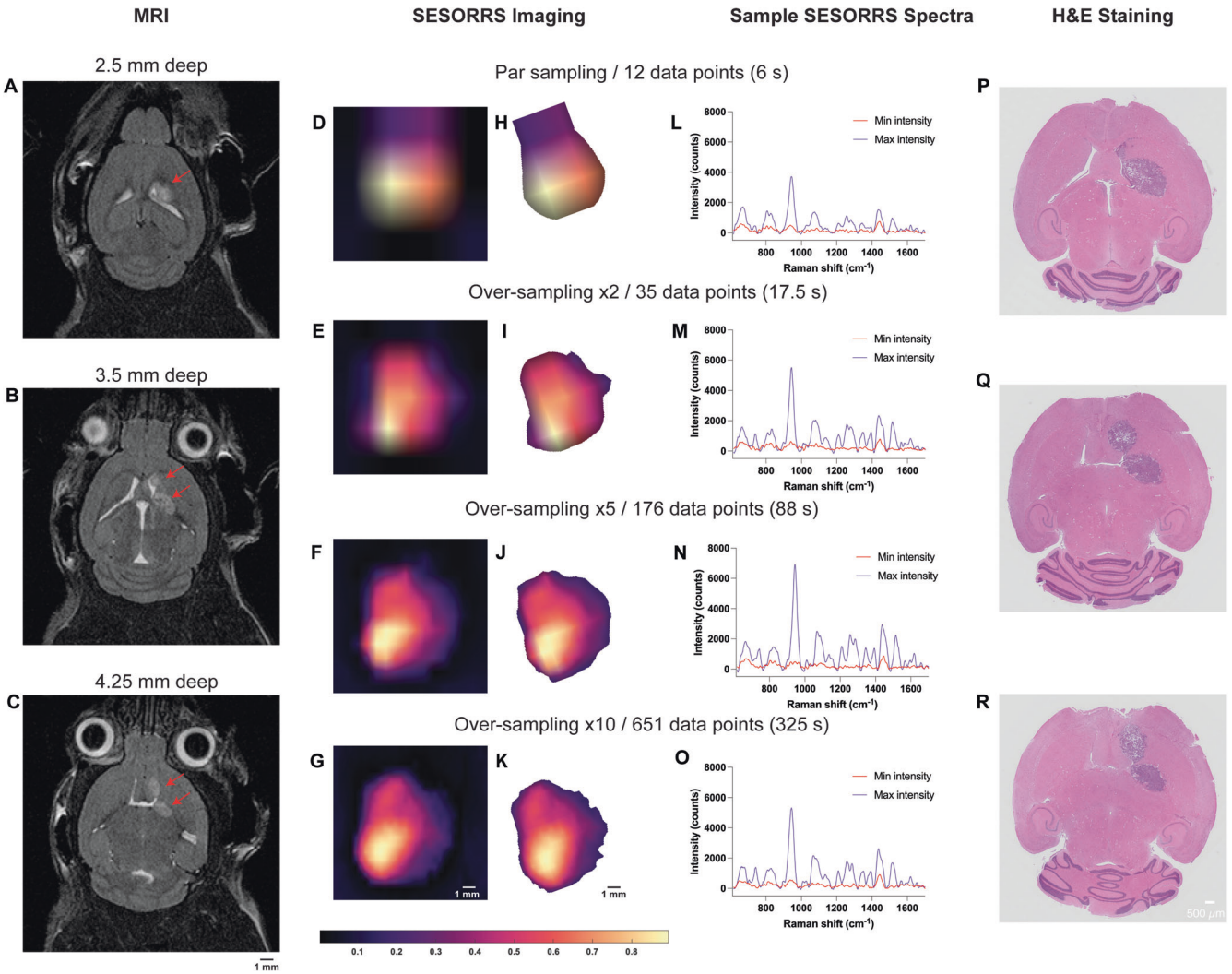

Fig. 6 | Representative imaging of GBM in mice ($n = 3$) using SESORS and optimized sampling approaches. A–C Magnetic resonance imaging at 2 weeks post-injection of GL261-Luc cells confirms the presence of a tumor as indicated by the red arrows. Magnetic resonance images acquired at depths of 2.5 mm, 3.5 mm, and 4.25 mm respectively. MR images demonstrate the emergence of a secondary tumor region at greater depths within the brain. Following confirmation of tumor growth, non-targeted SERRS NPs were administered to tumor-bearing mice (2 nM, 100 μL) via the tail vein. In vivo SESORRS imaging was performed using a spatial offset of 1.5 mm, using (**D**) par sampling frequency (12 data points) (**E**) over-sampling frequency of: 2 (35 data points), (**F**) 5 (176 data points), and (**G**) 10 (651 data points). The respective times taken to acquire each image are also shown. Raman spectra were truncated, normalized, and principal component (PC) analysis was applied to generate false-color 2D heat maps. PC scores 2 and 3 were used to create SESORS images and represent the accumulation of SERRS NPs in the tumor. SESORRS measurements were acquired using a power density of 6.5 mW/mm^2, 1.5 mm spatial offset, 0.5 s integration time, 1 acquisition, 785 nm excitation wavelength. **H–K** Background removal of areas of non-intensity from the SESORRS images. Images were then rotated to match the orientation of the MR images. **L–O** SESORRS spectra taken at the point of minimum and maximum intensity from the respective SESORRS image using a par sampling frequency and an oversampling frequency of 2, 5 and 10 respectively. **P–R** H&E stained 5 μM section of the brain confirming the presence of a tumor and the emergence of a secondary tumor region as deeper regions are sliced.

four sampling frequencies. In this case, the development of tumor grown in the deeper-seated area was spontaneous, meaning we did not purposely create two regions through the intracranial injection of mice with GL261-Luc cells. This is representative of an in vivo system in which tumor growth is spontaneous and heterogenous in nature. With this in mind, we believe that when looking to the future, SESORRS imaging could be applied for the intra-operative assessment of ROIs using this sampling frequency approach and may offer a benefit over current image guided surgical approaches. Following tumor resection, it is well established that microscopic malignant lesions are often missed by visual inspection. Currently, fluorescence probes lead the way in image guided surgical applications[4], however, both fluorescence and traditional SERRS approaches are only able to image superficial lesions of interest. Moreover, fluorescence imaging suffers from photobleaching and intrinsic autofluorescence[8]. Surgical resection is stopped once the surgeon is confident all malignant lesions have been removed, however there is a possibility that deep-seated, microscopic lesions remain due to the inability of fluorescence imaging to detect deep-seated lesions. Thus, we believe that it could be possible to apply SESORRS imaging using a par-sampling frequency to scan large areas of tissue to identify ROIs where the malignant tissues are present. Then, using a higher-sampling frequency approach, e.g. 2 or 5, delineate that same ROI with greater certainty and identify the presence of potentially deeper-seated lesions in real time. Future work will therefore focus on developing this approach through the incorporation of a white light camera to correlate what is seen by the naked eye with the corresponding SESORRS image, evaluating the efficiency of SESORRS–image guided surgery for the detection of deeper-seated lesions, i.e., determining signal contribution relative to depth in vivo using a multi-modal imaging approach. In this instance a spatial offset of 1.5 mm was used for SORS imaging, however it

is reasonable to assume that the other spatial offsets would have been suitable for SESORS imaging, e.g., 1, 2 and 2.5 mm. This is of course dependent on the sample under study it is reasonable to assume that the use of larger spatial offsets may lead to the detection of even deeper-seated ROI however this would come at the expense of spectral resolution and may require longer integration times. Other suggestions for future work include performing SESORRS imaging without prior knowledge of the tumor location as well as using computational modelling to better understand light propagation in media. The use of computational modelling approaches such as Monte Carlo simulations, or NIRFAST software, offer the potential to select optimal positions, and angles, for the incident beam and collection probes which are specific to the tissue, e.g., brain, under investigation[53].

Through improvements in the collection efficiency of our imaging probe, and consideration of sampling frequency approach, we demonstrate the ability to detect image GBM through the intact skull using a SESORRS approach. We demonstrate that in comparison to previous reports, the ability to identify and delineate a ROI can in fact be carried out relatively quickly and does not rely on such time-intensive measurement. To the best of our knowledge, no one has applied this approach for the in vivo imaging of cancer using conventional Raman, SERRS, SORS or SESORRS approaches. Importantly our results demonstrate the ability to detect deeper-seated tumors in agreement with MRI and histopathology in a much shorter timeframe than what has been previously reported. Moreover, the work presented here is the first to identify a secondary ROI using a SESORRS approach for the detection of cancer in vivo. Unlike other optical imaging approaches, SESORRS offers the opportunity to image deeper into tissue. We believe that the approach outlined here opens the potential for SESORRS to be applied in image-guided applications for the detection of multiple solid tumor types and demonstrates an important step forward in the development and application of SESORRS imaging for the detection of cancer in vivo.

Methods

Reagents

All chemicals were purchased from Sigma-Aldrich and used as received unless otherwise stated. Paraformaldehyde (16%) was purchased from Thermofisher and diluted to 4% in phosphate buffered saline (pH 7.1). Deionized water (DI), 18 MΩ·cm, was used in all experiments.

SERRS nanotag synthesis

SERRS nanotags were synthesized according to a protocol based on recent publications by our group, with minor modifications as detailed below[14,28].

Synthesis of gold seeds

5 nm gold seeds were synthesized in accordance with our previously described protocol[42]. 2 ml of 25 mM aqueous solution of $HAuCl_4$ were added to 200 ml of DI water. Afterwards, 6 ml of freshly-prepared ice-cold 100 mM $NaBH_4$ aqueous solution was added to the mixture under stirring and left overnight at room temperature before use.

Synthesis of bare gold nanostars

The seed-mediated synthesis of gold nanostars was performed in a cold room (+4 °C). To 1800 ml of 200 mM solution of ascorbic acid, 5 ml of gold seeds from previous step were added, followed by 2.5 ml of 400 mM solution of $HAuCl_4$. The obtained deep blue solution was rapidly transferred to 50 ml Falcon tubes and centrifuged at 0 °C and 3300 × g for 20 mins. After centrifugation, the transparent supernatant was removed and the liquid pellets on the bottom of the tubes were combined in a 15 ml Slide-A-Lyser G2 dialysis cassette with 20k MWCO and dialyzed in DI water. The water was changed daily over the 72-h timeframe.

Simultaneous Raman reporter attachment and silica encapsulation

To a 50 ml falcon tube (tube A), 1.2 ml of tetraethyl orthosilicate, 30 ml of isopropanol and 0.16 ml of 20 mM IR780p dye solution in DMF were added together. To a 15 ml falcon tube (tube B), 4 ml of 1 nM bare nanostars and 9 ml of ethanol were added. Immediately before combining tube A and tube B, 0.6 ml of ammonium hydroxide solution (28% aq) was added to tube B and tube B was shaken by rotation. The contents of tube B were added rapidly to tube A and the resulting mixture was left on a shaker for 20 min at room temperature. Next, tube A contents were divided equally between two 50 ml falcon tubes, which were each then filled with ethanol to 50 ml to quench the reaction, and then centrifuged at 3300 × g at 0 °C for 20 min. The dark green supernatant was removed, leaving ~0.5 ml of solutions with dark blue liquid pellets on the bottoms of the tubes. The pellets were sonicated to fully homogenize the solution and transferred to two 1.5 ml Protein LoBind Eppendorf tubes, which were then filled with ethanol. The tubes were centrifuged at 10000 × g at room temperature for 5 min and the supernatants were discarded. The resulting pellets were then resuspended in 1 ml of ethanol and subjected to sonication. Ethanol washing was repeated three more times.

Surface modification with PEG

To each 1 ml solution of nanostars resuspended in ethanol from the previous step, 0.1 ml of (3-mercaptopropyl)-trimethoxysilane and 0.04 ml of ammonium hydroxide solution (28% aq) were added and the reaction mixture was left on a shaker for 1 h at room temperature. Then they were centrifuged at 10000 × g at room temperature for 5 min, washed with ethanol three times as described above, washed once with water, and then each resuspended in 1 ml of 10 mM HEPES buffer pH 7.3 to obtain thiolated nanostars solutions. PEG5k-Mal (Sigma-Aldrich 63187, CAS 99126-64-4) was dissolved in anhydrous DMSO at the concentration of 20 mg/ml. 0.1 ml of this DMSO solution of PEG was added to each of the two solutions of thiolated nanostars in 10 mM HEPES buffer pH 7.3 to create a ~200,000:1 PEG/NPs ratio. The Eppendorf tubes were left on a shaker for 1 h at room temperature. The nanoparticles were spun down and washed 3 times with water and then resuspended in 10 mM HEPES buffer pH 7.3. Prior to injection, the nanoparticles were concentrated to 2 nM by spinning down the pellets, combining them, and resuspending in 1 ml of HEPES.

SERRS nanoparticle characterization

Transmission electron microscopy (TEM) was performed using a JEOL 1200EX Transmission Electron Microscope at 80 kV. The sample was prepared as follows: 1 µL of ~0.1 nM nanoparticles solution was left to dry onto a TEM grid (CF300-Cu, Electron Microscopy Sciences) for 30 min. Zeta potential measurements were performed using Zetasizer Nano ZS (Malvern) on particles dispersed in 10 mM HEPES buffer (pH 7.3). Nanoparticle tracking analysis (NTA) NS500 (Malvern) was used to determine nanoparticle concentration. UV2600 (Shimadzu) was used for optical characterization of nanoparticles.

Animal models

All animal experiments were approved by the Institutional Animal Care and Use Committees of Dana-Farber Cancer Center (protocol #08023). GL261-Luc cells were used to generate the tumor bearing mice. Briefly, 8 week-old BALB/cJ mice were injected intracranially with 100,000 GL261-Luc cells into the left striatum. Tumor incidence and size was determined by MRI (Bruker BioSpec 7 T/30 cm USR horizontal bore Superconducting Magnet System, Bruker Corp., Billerica, MA) 2 weeks after injection of GL261-Luc cells.

Custom-built SORS collection probe

All SORS in vivo measurements were carried out using a custom built SORS collection probe.

Custom-built SORS imaging system

All SORS measurements were carried out using a system built in house, the design of which was based on previous reports in the literature[45]. A 785 nm laser (Innovative Photonic Solutions) was coupled to a fiber optic probe (Innovative Photonic Solutions) and the lens was removed from the probe to enable the delivery of a diffuse collimated beam to the sample surface. Both the excitation and collection probe were mounted on individual *xyz* translational stages (Thorlabs) and a rotation mount was used to deliver the

excitation light to the sample at a 45° angle. The incident beam was set to intersect the sample surface at a 45° angle and was therefore elliptical, with the shorter diameter being 4 mm and the longer 6 mm. The scattered Raman light was either collected by a previously reported, commercially available collection probe[28] or a custom built collection probe which was built to increase light collection efficiency (Fig. 1a). The custom probe was designed as follows: The generated scattered Raman light was collected using a 0.34 NA lens (Thorlabs) and passed through two 785 nm dichroic beam-splitters (Semrock) angled at 45° mounted in cage cubes (Thorlabs). Two dichroic filters (instead of one) were used to reduce the Rayleigh and stray-light contributions. Light was then passed through a lens tube, an iris, and then a 785 nm longpass filter (Semrock) and an additional iris. The light was then passed through an additional 785 nm longpass filter (Semrock) positioned at 2° to eliminate the need for a custom filter and to further to increase the reflectance of unwanted incident-and stray-light, a collimator, and then a 400 μm, 0.34 numerical aperture (NA) core fiber (Thorlabs) where it was delivered to a high throughput f/2 spectrometer (Innovative Photonic Solutions), to collect the scattered Raman photons. The collection probe was mounted perpendicularly to the sample surface and had a working distance of 40 mm. The spatial offset was controlled by translating laser beam away from the focal point of the collection probe in the region of a few mm (Δx). This directed the beam at an appropriate point on the sample, e.g., plastic or mouse. All samples were positioned on a third translational *xy* stage (Thorlabs) to allow freedom to move the sample without impacting the alignment between the excitation and collection probes. The SORS system using the custom-built collection probe is shown in Fig. 1b.

SORS imaging parameters

Acquisition times and laser power were varied depending on the sample under study and are outlined below. Laser output was measured with a handheld laser power meter (Thorlabs). For SORS measurements using plastic phantoms a laser power of 500 mW was used. For brain tumor phantoms and animal models a laser power of 6 mW/mm^2 at the sample surface was applied.

SORS optimization measurements using plastic calibration standards

The efficiency of the custom built SORS collection probe in comparison to the previously used commercially available probe was evaluated using plastic calibration standards[28]. Polytetrafluoroethylene (PTFE) and pink polypropylene (PP) sheets were purchased from a plastic retailer. PTFE (5 cm (length) × 2 cm (width) × 2 mm (thickness)) was placed on the stage and varying numbers of PP sheets (length 5 cm × width 2 cm × thickness 2 mm) were then placed on top of the PTFE to act as a barrier (Fig. S1A, supporting information). Their corresponding Raman spectra are shown in the supporting information (Fig. S1B,C). To increase the thickness of the barrier, further PP sheets were added. Measurements were carried out using a 4 s integration time, one accumulation, 500 mW, 785 nm laser. The spatial offset was controlled by moving the *xyz* translation stage coupled to either of the collection probes (commercially available or custom built) in the *x* direction.

SORS optimization measurements using brain tumor phantoms

A brain tumor phantom was prepared using the head of a healthy 12-week-old-euthanized mouse. The brain was removed, and a small piece of PTFE (5 × 5 mm) was placed under the skull and glued in place. The skull was then filled with 1% agarose gel to create a phantom[47]. Unlike previous reports, the skin was not removed from the skull in order to create a more realistic phantom. Paraffin wax was melted using a heat plate and poured into a small plastic weigh boat. After the wax had partially cooled, the mouse's head was positioned atop the semi-solid paraffin, which served as a mold for the base of the rodent's cranium. The weigh boat containing the molded paraffin wax was then fixed in position on the *xy* translational stage. This allowed for consistent measurements of the mouse's head over multiple days, ensuring that the head was positioned identically to the previous day. SORS measurements were carried out with the custom-built system at spatial offsets of 1, 1.5, 2, 2.5, and 3 mm. Again, the spatial offset distance was controlled by moving the *xyz* translation stage in the *x* direction. Measurements were acquired using different sampling frequencies (par sampling, 2× oversampling, 5× oversampling, and 10× oversampling). Spectra were obtained using a 0.5 s integration time, one accumulation, 6 mW/mm^2, 785 nm. The step size used for each Raman map was dependent on the sampling frequency applied. Step sizes of 6 mm × 4 mm, 3 mm × 2 mm, 1.2 mm × 0.8 mm and 0.6 mm × 0.4 mm were used for a par-sampling, 2× oversampling, 5× oversampling, and 10× oversampling respectively. Step sizes for each sampling frequency were determined by the laser spot size (6 mm × 4 mm) and described in Table 1.

Imaging of GBM using SESORS

Prior to imaging, mice were shaved using an electric shaver and residual hair removed using hair removal cream. Each mouse was placed onto the *xy* translational stage with a range of 50 mm in each direction and moved in varying step sizes specific to each sampling frequency to acquire pointwise spectra. Mice ($n = 3$) were injected via the tail vein with 2 nM SERRS CAs suspended in HEPES. Imaging was performed approximately 18 h post injection of SERRS CAs.

Biodistribution studies of SERRS CAs

Biodistribution analysis was performed to determine the fate of the SERRS nanotags in vivo. GBM-bearing mice ($n = 3$) were injected with 2 nM of SERRS contrast agents (100 μL). Following administration, mice were euthanized using CO2 asphyxiation approximately 18 h post injection. For each mouse ($n = 3$), tissues were harvested, weighed, and homogenized. Tissue homogenates were placed in 384-well plates. Raman images of the plates were acquired using 10% laser power (785 nm), 1 s acquisition, 5× objective (LabRAM HR Evolution (HORIBA Scientific. Spectra were baseline corrected, normalized to the maximum peak intensity, and the peak intensity at 947 cm^{-1} was plotted as a combination surface/contour false color 2D heat map. The peak at 947 cm^{-1} was selected since it is the strongest peak in the SERRS spectrum.

Histology

Intact GBM-bearing brains were fixed in 4% paraformaldehyde (PFA) for 24 h, transferred to 70% ethanol, and then embedded in paraffin. Each brain was sliced in the same orientation as the MRI and 5 μm-thick sections were stained with hematoxylin and eosin (H&E). Images were acquired using an Olympus BX-UCB slide scanner with a 20× objective and processed using OMERO software.

Data processing

All spectra were processed using MATLAB software (version 2022b, The MathWorks) and LabSpec (version 6.6.2.7, HORIBA Scientific). SNRs were calculated by baselining the spectra and dividing the peak height of PTFE at 739 cm^{-1} by the intensity of the noise across 1799 cm^{-1} to 1899 cm^{-1}. Processing of individual reference spectra involved truncating, and baseline correcting the spectra, followed by Savitzky–Golay smoothing. For the creation of false color 2D heat maps using brain tumor phantoms, spectra were truncated, baseline corrected, and smoothed using Savitzky–Golay filtering using MATLAB. The intensity of the peak at 739 cm^{-1} was then plotted as a combination surface/contour false color 2D heat map. For in vivo SESORRS images, spectra were truncated, baseline corrected using a polynomial fit and normalized using standard normal variate method in LabSpec. The in vivo SESORRS spectral data had poorer SNR and higher background fluorescence compared to the phantom data. This meant that we couldn't simply plot the maximum peak intensity of the SERRS CAs as a false color heatmap and instead had to apply multivariate analysis. Principal component analysis (PCA) was therefore applied using the MVA-EVRI toolbox in LabSpec. Principal components (PC) 2 and 3 were folded to produce the spectral image. The intensity of peak height over the region of 898 cm^{-1} to 990 cm^{-1} was plotted and the data were extracted and

transferred to MATLAB where they were plotted as combination interpolated/bilinear false color 2D heat maps.

In addition, we developed an in-house Python-based GUI for processing heat maps following PCA. The tool automatically identifies pixels in an image where the RGB values are all below 100, indicating they are a shade of black, and replaces them with a transparent pixel. This is achieved without altering the original dimensions of the heatmap. The process involved loading an image, applying the transparency adjustment, and saving the processed image. The GUI provides a user-friendly interface to choose an image, make black pixels transparent, and save the processed image. The code leverages the tkinter library for GUI creation and the Python Imaging Library (PIL) for image processing.

Data availability

Data is available upon reasonable request to the corresponding author.

Received: 20 September 2023; Accepted: 8 February 2024;
Published online: 03 April 2024

References

1. Pirovano, G., Roberts, S., Kossatz, S. & Reiner, T. Optical imaging modalities: principles and applications in preclinical research and clinical settings. *J. Nucl. Med.* **61**, 1419 (2020).
2. Ran, C. et al. Practical guidance for developing small-molecule optical probes for in vivo imaging. *Mol. Imaging Biol.* **25**, 240–264 (2023).
3. Pysz, M. A., Gambhir, S. S. & Willmann, J. K. Molecular imaging: current status and emerging strategies. *Clin. Radiol.* **65**, 500–516 (2010).
4. Hartshorn, C. M. et al. Nanotechnology strategies to advance outcomes in clinical cancer care. *ACS Nano* **12**, 24–43 (2018).
5. Barth, C. W. & Gibbs, S. L. Fluorescence image-guided surgery - a perspective on contrast agent development. *Proc. SPIE Int. Soc. Opt. Eng*. **11222**, 112220J (2020).
6. Lauwerends, L. J. et al. The complementary value of intraoperative fluorescence imaging and Raman spectroscopy for cancer surgery: combining the incompatibles. *Eur. J. Nucl. Med. Mol. Imaging* **49**, 2364–2376 (2022).
7. Hernandez Vargas, S. et al. Specific targeting of somatostatin receptor subtype-2 for fluorescence-guided surgery. *Clin. Cancer Res.* **25**, 4332–4342 (2019).
8. Harmsen, S. et al. Surface-enhanced resonance Raman scattering nanostars for high-precision cancer imaging. *Sci. Transl. Med.* **7**, 271ra7–271ra7 (2015).
9. Cordero, E., Latka, I., Matthäus, C., Schie, I. & Popp, J. In-vivo Raman spectroscopy: from basics to applications. *J. Biomed. Opt.* **23**, 1–23 (2018).
10. Masson, L. E. et al. Dual excitation wavelength system for combined fingerprint and high wavenumber Raman spectroscopy. *Analyst* **143**, 6049–6060 (2018).
11. Matthäus, C. et al. Detection and characterization of early plaque formations by Raman probe spectroscopy and optical coherence tomography: an in vivo study on a rabbit model. *J. Biomed. Opt.* **23**, 1–6 (2018).
12. Jermyn, M. et al. Intraoperative brain cancer detection with Raman spectroscopy in humans. *Sci. Transl. Med.* **7**, 274ra19 (2015).
13. Butler, H. J. et al. Using Raman spectroscopy to characterize biological materials. *Nat. Protoc.* **11**, 664–687 (2016).
14. Harmsen, S. et al. Detection of premalignant gastrointestinal lesions using surface-enhanced resonance raman scattering-nanoparticle endoscopy. *ACS Nano* **13**, 1354–1364 (2019).
15. Harmsen, S. et al. Rational design of a chalcogenopyrylium-based surface-enhanced resonance Raman scattering nanoprobe with attomolar sensitivity. *Nat. Commun.* **6**, 6570 (2015).
16. Harmsen, S., Wall, M. A., Huang, R. & Kircher, M. F. Cancer imaging using surface-enhanced resonance Raman scattering nanoparticles. *Nat. Protoc.* **12**, 1400–1414 (2017).
17. Andreou, C. et al. Surface-enhanced Resonance Raman Scattering Nanoprobe Ratiometry for Detecting Microscopic Ovarian Cancer via Folate Receptor Targeting. J. Vis. Exp. https://doi.org/10.3791/58389 (2019).
18. Oseledchyk, A., Andreou, C., Wall, M. A. & Kircher, M. F. Folate-targeted surface-enhanced resonance raman scattering nanoprobe ratiometry for detection of microscopic ovarian cancer. *ACS Nano* **11**, 1488–1497 (2017).
19. Qian, X. et al. In vivo tumor targeting and spectroscopic detection with surface-enhanced Raman nanoparticle tags. *Nat. Biotechnol.* **26**, 83–90 (2008).
20. Davis, R. M. et al. A Raman Imaging Approach Using CD47 Antibody-Labeled SERS nanoparticles for identifying breast cancer and its potential to guide surgical resection. *Nanomaterials (Basel)* **8**, 953 (2018).
21. Huang, R. et al. High precision imaging of microscopic spread of glioblastoma with a targeted ultrasensitive SERRS molecular imaging probe. *Theranostics* **6**, 1075–1084 (2016).
22. Gao, X. et al. Guiding Brain-Tumor Surgery via Blood-Brain-Barrier-Permeable Gold Nanoprobes with Acid-Triggered MRI/SERRS Signals. *Adv. Mater.* **29**, 1603917 (2017).
23. Maeda, H., Wu, J., Sawa, T., Matsumura, Y. & Hori, K. Tumor vascular permeability and the EPR effect in macromolecular therapeutics: a review. *J. Control Rel.* **65**, 271–284 (2000).
24. Kircher, M. F. et al. A brain tumor molecular imaging strategy using a new triple-modality MRI-photoacoustic-Raman nanoparticle. *Nat. Med.* **18**, 829–834 (2012).
25. Zavaleta, C. L. et al. Multiplexed imaging of surface enhanced Raman scattering nanotags in living mice using noninvasive Raman spectroscopy. *Proc. Natl. Acad. Sci. USA* **106**, 13511–13516 (2009).
26. Andreou, C. et al. Imaging of liver tumors using surface-enhanced raman scattering nanoparticles. *ACS Nano* **10**, 5015–5026 (2016).
27. Eremina, O. E. et al. Expanding the multiplexing capabilities of raman imaging to reveal highly specific molecular expression and enable spatial profiling. *ACS Nano* **16**, 10341–10353 (2022).
28. Nicolson, F. et al. Non-invasive in vivo imaging of cancer using surface-enhanced spatially offset raman spectroscopy (SESORS). *Theranostics* **9**, 5899–5913 (2019).
29. Matousek, P. et al. Subsurface probing in diffusely scattering media using spatially offset Raman spectroscopy. *Appl. Spectrosc.* **59**, 393–400 (2005).
30. Nicolson, F., Kircher, M. F., Stone, N. & Matousek, P. Spatially offset Raman spectroscopy for biomedical applications. *Chem. Soc. Rev.* **50**, 556–568 (2021).
31. Mosca, S. et al. Determination of inclusion depth in ex vivo animal tissues using surface enhanced deep Raman spectroscopy. *J Biophotonics* **13**, e201960092 (2020).
32. Mosca, S., Conti, C., Stone, N. & Matousek, P. Spatially offset Raman spectroscopy. *Nat. Rev. Meth. Primers* **1**, 21 (2021).
33. Stone, N. et al. Surface enhanced spatially offset Raman spectroscopic (SESORS) imaging – the next dimension. *Chem. Sci.* **2**, 776–780 (2011).
34. Berry, M. E. et al. Tomographic imaging and localization of nanoparticles in tissue using surface-enhanced spatially offset raman spectroscopy. *ACS Appl. Mater. Interfaces* **14**, 31613–31624 (2022).
35. Zhang, Y. et al. In vivo surface-enhanced transmission raman spectroscopy under maximum permissible exposure: toward photosafe detection of deep-seated tumors. *Small Methods* **7**, e2201334 (2023).

36. Dey, P. et al. Surface enhanced deep Raman detection of cancer tumour through 71 mm of heterogeneous tissue. *Nanotheranostics* **6**, 337–349 (2022).
37. Mosca, S. et al. Spatially offset raman spectroscopy—how deep? *Anal. Chem.* **93**, 6755–6762 (2021).
38. Moody, A. S., Baghernejad, P. C., Webb, K. R. & Sharma, B. Surface enhanced spatially offset raman spectroscopy detection of neurochemicals through the skull. *Anal. Chem.* **89**, 5688–5692 (2017).
39. Moody, A. S., Payne, T. D., Barth, B. A. & Sharma, B. Surface-enhanced spatially-offset Raman spectroscopy (SESORS) for detection of neurochemicals through the skull at physiologically relevant concentrations. *Analyst* **145**, 1885–1893 (2020).
40. Nicolson, F. et al. Multiplex imaging of live breast cancer tumour models through tissue using handheld surface enhanced spatially offset resonance Raman spectroscopy (SESORRS). *Chem. Commun. (Camb)* **54**, 8530–8533 (2018).
41. Nicolson, F. et al. Through tissue imaging of a live breast cancer tumour model using handheld surface enhanced spatially offset resonance Raman spectroscopy (SESORRS). *Chem. Sci.* **9**, 3788–3792 (2018).
42. Wall, M. A. et al. Surfactant-free shape control of gold nanoparticles enabled by unified theoretical framework of nanocrystal synthesis. *Adv. Mater.* **29**, 1605622 (2017).
43. Everall, N. J. Confocal Raman microscopy: common errors and artefacts. *Analyst* **135**, 2512–2522 (2010).
44. Lee, E. Imaging Modes. In *Raman Imaging: Techniques and Applications* (ed. Zoubir, A.) 1–37. https://doi.org/10.1007/978-3-642-28252-2_1 (Springer Berlin Heidelberg, 2012).
45. Everall, N. et al. Optimizing depth resolution in confocal raman microscopy: a comparison of metallurgical, dry corrected, and oil immersion objectives. *Appl. Spectrosc.* **61**, 251–259 (2007).
46. Pal, S. et al. DNA-enabled rational design of fluorescence-Raman bimodal nanoprobes for cancer imaging and therapy. *Nat. Commun.* **10**, 1926 (2019).
47. Thakor, A. S. et al. The fate and toxicity of Raman-active silica-gold nanoparticles in mice. *Sci. Transl. Med.* **3**, 79ra33 (2011).
48. Kenry et al. Advances in surface enhanced raman spectroscopy for in vivo imaging in oncology. *Nanotheranostics* **6**, 31–49 (2022).
49. Milligan, J. J. & Saha, S. A nanoparticle's journey to the tumor: strategies to overcome first-pass metabolism and their limitations. *Cancers (Basel)* **14**, 1741 (2022).
50. Cheng, Y.-H., He, C., Riviere, J. E., Monteiro-Riviere, N. A. & Lin, Z. Meta-analysis of nanoparticle delivery to tumors using a physiologically based pharmacokinetic modeling and simulation approach. *ACS Nano* **14**, 3075–3095 (2020).
51. Campbell, J. L. et al. Multimodal assessment of SERS nanoparticle biodistribution post ingestion reveals new potential for clinical translation of Raman imaging. *Biomaterials* **135**, 42–52 (2017).
52. Wang, Z., Bovik, A. C., Sheikh, H. R. & Simoncelli, E. P. Simoncelli. Image quality assessment: from error visibility to structural similarity. *IEEE Trans. Image Processing* **13**, 600–612 (2004).
53. Dooley, M. et al. Model-based optimization of laser excitation and detection improves spectral contrast in noninvasive diffuse raman spectroscopy. *Appl. Spectrosc.* **76**, 801–811 (2022).

Acknowledgements

We acknowledge the initial contributions of Moritz F. Kircher (MFK), MD, PhD who passed away during the initial stages of this work. This paper is dedicated to his memory. This work was supported by the following grants: DFCI start-up funds awarded to M.F.K.; DFCI Trustee Science Committee Postdoctoral Fellowship, Claudia Adams Barr Award for Innovative Cancer Research (DFCI), K99CA266921 and R00CA266921 to F.N.; an award from the Cancer Research UK Grand Challenge and the Mark Foundation to K.M.H. and the SPECIFICANCER team; TAMU and TEES start-up funding, NSF-Engineering Research Center for Precise Advanced Technologies and Health Systems for Underserved Populations (PATHS-UP)-Award Number 1648451, and NSF Funding Award Number: 2022805 to S.M; NCI-CaNCURE program, award number 5R25CA174650 to N.R. We also thank the pre-clinical animal imaging core facility (Lurie Family Imaging Center, Dana-Farber Cancer Institute) for technical assistance and advice. Figures 1 and 5 were created in part, using Biorender.com.

Author contributions

F.N., B.A., E.L., B.O., N.R., D.L.B., A.C., A.P., S.R., S.M., conducted and planned experiments, analyzed the data, and wrote the manuscript. A.W., J.Y., K.M.H., designed experiments, analyzed the data, and wrote the manuscript. All authors reviewed the manuscript prior to submission.

Competing interests

S.R. has several pending patents in the areas of Wavelength Stabilized Lasers, Raman Probes, Raman Concatenation, dual wavelength lasers for fluorescence mitigation and fluid analysis using Raman spectroscopy.

Additional information

Supplementary information The online version contains supplementary material available at https://doi.org/10.1038/s44303-024-00011-9.

Correspondence and requests for materials should be addressed to Fay Nicolson.

Fay Nicolson[1,2] ✉, Bohdan Andreiuk[2,3], Eunah Lee[4], Bridget O'Donnell[4,5], Andrew Whitley[4], Nicole Riepl[6], Deborah L. Burkhart[1], Amy Cameron[2], Andrea Protti[2], Scott Rudder[7], Jiang Yang[8], Samuel Mabbott[9,10] & Kevin M. Haigis[1]

[1]Department of Cancer Biology, Dana-Farber Cancer Institute and Harvard Medical School, Boston, MA 02215, USA. [2]Department of Imaging, Dana-Farber Cancer Institute and Harvard Medical School, Boston, MA 02215, USA. [3]Cancer Immunology and Virology, Dana-Farber Cancer Institute and Harvard Medical School, Boston, MA 02215, USA. [4]HORIBA Instruments Incorporated, Piscataway, NJ 08854, USA. [5]Honeywell International Inc., Fort Washington, PA 19034, USA. [6]College of Science, Northeastern University, 360 Huntington Avenue, Boston, MA 02115, USA. [7]Innovative Photonic Solutions, Monmouth Junction, Plainsboro Township, NJ 08852, USA. [8]State Key Laboratory of Oncology in South China, Collaborative Innovation Center for Cancer Medicine, Sun Yat-sen University Cancer Center, Guangzhou, China. [9]Department of Biomedical Engineering, Texas A&M University, Emerging Technologies Building, College Station, TX 77840, USA. [10]Center for Remote Health Technologies & Systems, Texas A & M Engineering Experiment Station, 600 Discovery Drive, College Station, TX 77840, USA.
✉e-mail: fay_nicolson@dfci.harvard.edu